

Design, synthesis, and greener pasture biological assessment of a novel nucleoside: 1-(α -D-ribofuranosyl)-6,7-difluoro-2-methyl-4-quinazolinone as an inhibitor of COVID-19 and Alzheimer's disease

Laila M. BREAK¹ , Adil A. GOBOURI¹ , Wafa S. AI-HSRTHI¹ , Mohamed HAGAR² , Nadia S. AI-KAFF³ ,
Musa A. SAID^{4,5,*} 

¹Department of Chemistry, College of Science, Taif University, Taif, Saudi Arabia

²Department of Chemistry, Faculty of Science, Alexandria University, Alexandria, Egypt

³Biology Department, College of Science, Taibah University, Al-Madinah Al-Munawara, Saudi Arabia

⁴Chemistry Department, College of Science, Taibah University, Al-Madinah Al-Munawara, Saudi Arabia

⁵Institute of Inorganic Chemistry, University of Stuttgart Pfaffenwaldring, Stuttgart, Germany

Received: 12.02.2022 • Accepted/Published Online: 16.06.2022 • Final Version: 19.12.2022

Abstract: Synthesis of a new fluorinated nucleoside of 6,7-difluoro-2-methyl-4-quinazolinone was described. 2-Amino-4,5-difluorobenzoic acid **1** reacts with $(\text{CH}_3\text{CO})_2\text{O}$ followed by ammonia to form (1*H*)-6,7-difluoro-2-methyl-4-quinazolinone **3a**. Ribosylation of a silylated **4** with 1-*O*-acetyl-2,3,5-tri-*O*-benzoyl- α -D-ribofuranose **5** forms a protected nucleoside **6** then unprotected from **6** to give a free nucleoside **7**. Greener pasture biological docking of the cystine protease of COVID-19 [M^{pro}, code 7BQY, PDB] by novel nucleoside and fluoroquinazoline compounds is presented. LIGPLOT (2D) representations calculated for the same ligands are shown. A superposition of remdesivir approved medicine, **N3** inhibitor, and our ligands docked together into the binding protein of 7BQY is also given for a fair comparison. The binding affinities of remdesivir, **N3** inhibitor, the nucleoside **7**, and fluoroquinazoline **3a**, **3b** compounds with 7BQY calculated under the same conditions are -7.7, -7.4, -7.6, -6.1, and -6.1 kcal mol⁻¹, respectively. The high values were due to the existence of many hydrophobic interactions and hydrogen bonds between the ligands and the active amino acid residues of the receptor, indicating a promising candidate as a COVID-19 inhibitor. Pro Tox -II server showed that compound **7** has a similar feature to the approved antiviral drug remdesivir for COVID-19. Additionally, a fascinating molecular modeling investigation showed that our nucleoside demonstrated good binding inhibition of AChE enzyme towards advancing an efficient medication against Alzheimer's disease. Finally, DFT has been conducted to illustrate the MD results in terms of the molecular descriptor-based structural activity relationship calculated from FMOs.

Key words: Main protease, in silico, MD-DFT assessment, Alzheimer's disease (AD), 6,7-difluoro-2-Methyl-4-quinazolinone

1. Introduction

4-quinazolinones are solids and stable to alkaline treatment and mild acid. The most common approach to synthesizing 4(3*H*)-quinazolinone products is the direct reaction of 2-aminobenzoic acid (anthranilic acid) derivatives with acetic anhydride to give the benzoxazinone, followed by condensation with nitrogen nucleophiles [1–4]. The 2-methyl group in 3*H* or 1*H*-4-quinazolinone is more responsive than 4-quinazolinone. In general, quinazolinones have several biological applications such as preventing cancer [2,5,6], anti-HIV [7], cytotoxicity in vitro [8], antiinflammatory [6,9], antibacterial [10,11], antifungal [12], and antiviral properties [13,14]. Furthermore, the kinase inhibitory potency of many N-aryl thiazolo[5,4-*f*]quinazolin-4-amines has been revealed, intending to improve the healing of Down syndrome (DS) and early AD [15–18]. The fluorine atom is a significant substituent in medicinal chemistry due to its electronic properties and improved molecular lipophilicity [19]. New fluorinated hydroquinazolinone derivatives were used as antifungal agents [20] and anticancer agents [21]. A difluorinated inhibitor showed 4.23 times larger potency against the epidermal growth factor receptor (EGFR) than a nonfluorinated inhibitor [22] mutations of which have been linked specifically to non-small-cell lung cancer. For the L858R/T790M/C797S triplet mutant (EGFRTM). In addition, quinazolinone nucleosides [23–26] and fluorinated nucleosides have been used extensively in biological activity such as the prevention of cancer cells from forming, anti-HCV activity in vitro [27], and anti-HBV agents [28].

* Correspondence: masaid@taibahu.edu.sa

This article aims to report a new fluorinated nucleoside quinazolinone containing two fluorine atoms at positions 6 and 7 of the quinazolinone moiety [29]. When this compound was reacted with 1-*O*-acetyl-2,3,5-tri-*O*-benzoyl- β -D-ribofuranose **5** by silylated method [30], the fluorinated nucleoside; 6,7-difluoro 2-methylquinazolin-4-one **7** was obtained. Also, given the current several ongoing concerns in medicine finding to monitor the horrific effect of the virus on our daily lives [3,31–33], we have been encouraged to screen, *in silico* as a greener pasture preliminary step, the interaction between our novel nucleoside: 1-(2,3,5-tri-*O*-benzoyl- β -D-ribofuranosyl)-6,7-difluoro-2-methyl-4-quinazolinone, **7** and fluoroquinazoline, **3** ligands with the main protease (downloaded from RCSB, PDB) deposition code 7BQY) active site as possible candidate drugs for COVID-19. It is worth mentioning here that nucleoside was tested before, *in vitro*, for antiviral activity against two representative cowpox viruses, ortho poxviruses, and vaccinia virus [34]. We also investigated, *in silico*, the molecular modeling of our nucleoside as a binding inhibition of AChE enzyme towards the advancement of an efficient drug against Alzheimer's disease.

2. Materials and methods

TLC was done using silica gel 60 (aluminum sheet, Fluka company) and revealed by UV-vis light. Melting points (mp) of all synthesized compounds were determined using an electrothermal device and are uncorrected. The ^1H and ^{13}C NMR spectra were measured on an NMR spectrometer in CDCl_3 , CD_3OD at 213 and 850 MHz. Mass spectra were measured on GC MS-QP 2000 EX mass spectrometer at 70 e.V (King Abdel Aziz University).

2.1. Synthesis

Synthesis of 6,7-difluoro-2-methylbenzo[2,3-d]oxazin-4-one (2) 2-amino-4,5-difluorobenzoic acid **1** (1.6416 g, 0.009 mol) with a suitable quantity of acetic anhydride was refluxed for 1 h to reveal compound **2** as a brown powder. Yield: 1.6971 g (89.5%); mp: 158 °C; molecular formula: $\text{C}_9\text{H}_5\text{NO}_2\text{F}_2$; molecular weight (mol. wt): 197.13.

Synthesis of 1H-6,7-difluoro-2-methyl-4-quinazolinone (3a) 1.69 g (0.009 mol) of compound **2** with a suitable quantitative amount of ammonia solution was refluxed for 6 h, cooled, and then treated with acetic acid to give crystals collected by filtration as a white powder of compound **3a**. Yield: 0.3690 g (21.95%); mp: 263–270 °C; molecular formula: $\text{C}_9\text{H}_6\text{F}_2\text{N}_2\text{O}$, mol. wt: 196.15, MASS m/z (%): M^+ = 196.06 (100%), 196.04 (100%) [29,35].

Ribosylation of 1H-6,7-difluoro-2-methyl-4-quinazolinone:

1-(2,3,5-tri-*O*-benzoyl- β -D-ribofuranosyl)-6,7-difluoro-2-methyl-4-quinazolinone (6) A mixture of 1H-6,7-difluoro-2-methyl-4-quinazolinone **3a** (0.369 g, 0.0018 mol), dry HMDS (20 mL) and a catalytic quantity of $(\text{NH}_4)_2\text{SO}_4$ were heated under reflux for 24 h (TLC). The product was evaporated to dryness in anhydrous media to afford the silylated derivative **4** as an intermediate compound, which added (10 mL) of dry 1,2-dichloroethane, (0.4694 g, 0.9 mmol) 1-*O*-acetyl-2,3,5-tri-*O*-benzoyl- β -D-ribofuranose (**5**) and (2 mL, 10 mmol) trimethylsilyl triflate; (TMSOTf as a catalyst). The obtained solution was stirred for 14 days at room temperature and then washed with an aqueous NaHCO_3 followed by water and dried over sodium sulfate. The silica gel column chromatography with ethyl acetate and chloroform (2:98) was used in order to separate the pure product. After evaporation, the main fraction **6** was obtained as a sticky yellow material. Yield: 0.378 g (49.93%); mp: 180 °C; molecular formula: $\text{C}_{35}\text{H}_{26}\text{F}_2\text{N}_2\text{O}_8$; mol. wt: 640.59; ^1H NMR (CDCl_3 , 850 MHz, TMS), δ H: 8.06–7.13 (m, 17H Aromatic protons), 6.0–6.1 (d, 1H, $J = 4.25$ Hz, H-1'), 5.62 (t, $J = \text{Hz}$, 1H, H-2'), 4.97 (t, $J = \text{Hz}$, 1H, H-3'), 4.49–4.72 (m, 1H, H-5'), 4.01–4.06 (m, 1H, H-4'), 1.56 (s, 3H) CH_3 ; ^{13}C NMR (CD_3OD , 213 MHz, TMS), δ : 190.00, 167.63, 167.32, 164.32, 157.06, 155.73, 141.90, 138.05, 132.93, 132.87, 132.83, 130.57, 130.54, 129.71, 130.59, 129.92, 129.77, 129.74, 129.72, 129.50, 128.66, 128.43, 128.42, 128.40, 128.32, 128.29, 119.10; 117.75, 101.43, 79.16, 75.76, 70.25, 60.32, 65.14 CH_2 , 17.65 CH_3 .

Deprotection of 1-(2,3,5-tri-*O*-benzoyl- α -D-ribofuranosyl)-6,7-difluoro-2-methyl-4-quinazolinone-1-(α -D-ribofuranosyl)-6,7-difluoro-2-methyl-4-quinazolinone (7).

A mixture of compound **6** (0.5 mmol), and sodium metal (0.001g) in methanol (dry, 10 mL), 0.04 mmol) was stirred at room temperature for 1 day. It was then treated with drops of acetic acid to neutralize the solution. The residue was recrystallized from water to offer **7** as light-yellow crystals. Yield: 0.152 g (81.28%); mp: 255 °C; molecular formula: $\text{C}_{14}\text{H}_{14}\text{F}_2\text{N}_2\text{O}_5$, mol. wt: 328.27; ^1H NMR (CD_3OD , 850 MHz, TMS), δ : 7.88 (s, 1H, H-5'), 6.94 (s, 1H, H-8), 6.9 (d, 1H, $J = 6.80$ Hz, H-1'), 6.60–6.63 (m, 1H, H-2'), 5.65 (d, 1H, $J = 4.25$ Hz, OH2'), 5.33 (d, 1H, $J = 1.7$ Hz, OH3'), 5.18 (d, 1H, $J = 3.4$ Hz, OH5'), 4.70–4.95 (m, 3H, H-3', OH-3', OH-2'), 3.63–3.68 (m, 2H, H-4', OH-4'), 3.52 (t, $J_1 = 6.80$, $J_2 = 6.80$ Hz, 1H, H-5'), 1.88 (s, 3H, CH_3); ^{13}C NMR (CD_3OD , 213 MHz, TMS), δ : 160.0, 129.3, 128.8, 128.2, 127.2, 127.1, 126.0, 124.0, 78.0, 61.6, 51.2, 51.0, 50.9, 29.3; MASS m/z (%): M^+ = 327.21, 326.00, 322.24, 319.18 (100), 306.24, 301.10, 298.21, 293.98, 287.08, 279.07, 263.12, 260.05, 328.14, 252.20, 243.94, 232.96, 220.02, 203.96, 193.11, 190.90, 184.95, 171.95, 163.98, 155.16, 142.95, 123.99, 107.03, 102.90, 91.97. (calc. 328.27).

2.2. Docking in silico studies

The molecular docking studies of our nucleoside compound and donepezil were done using the PyRx 0.8 (<https://sourceforge.net/projects/pyrx/>). It is a recommended and powerful visualization engine [36] offering preprocessing and postprocessing adapted (to date). The settings in the PyRx 0.8 include: Grid box (19.61, 29.01, 36.27 Å³), (3.54, 64.29, 64.01 Å³) centered at (19.61, 29.10, 26.27), (23.06, 25.0, 25.0) for 7BQY and 1ELE. Energy range = 4 and exhaustiveness = 8. Water molecules and the N3 ligand were deleted from the proteases (PDB code 7BQY, 1EVE). The key residues of 7BQY used in this study were identified before [31, 37].

2.3. Molecular descriptor-based structural activity relationship calculated from FMOs

The optimal architectural structures of the synthesized compounds **3a**, **3b**, and **7** were computed in the gas phase using Gaussian 9 on the B3LYP 6-311G basis set and have been used in the calculation of the molecular chemical descriptors. The energy levels of the frontier molecular orbitals highest occupied molecular orbitals (HOMOs) and lowest occupied molecular orbitals (LUMOs) could be used to compute several chemical descriptors (least unoccupied molecular orbitals). Furthermore, HOMOs and LUMOs in the examined compounds could be used as a qualitative predictor of their ability to donate or receive electrons from the neighboring receptor [38–40]. FMOs, in general, are a powerful component for obtaining realistic qualitative data on excitation qualities in a variety of chemical and pharmacological processes [39,41–44]. Furthermore, FMO-derived chemical descriptors have been employed to estimate biological activities [45–54]. 4-dihydro-[1,2,4]triazole-3-thione was synthesized and structurally characterized by elemental analysis, FT-IR, Raman, ¹H and ¹³C-NMR and UV-Vis studies. A density functional theory (DFT). Likewise, the FMOs energy levels and the energy gaps may influence the kind and amount of binding during their interactions with receptors. As a result, nonbonding intermolecular interactions such as hydrophilic interactions and H-bonding occur with the receptor.

Table 1 presents many estimated thermodynamic molecular descriptors, including dipole moment (μ), electronegativity (χ), charge transfer prevention extent, global hardness (η), and electrophilicity (ω) determined from electronegativity and chemical hardness values.

3. Results and discussion

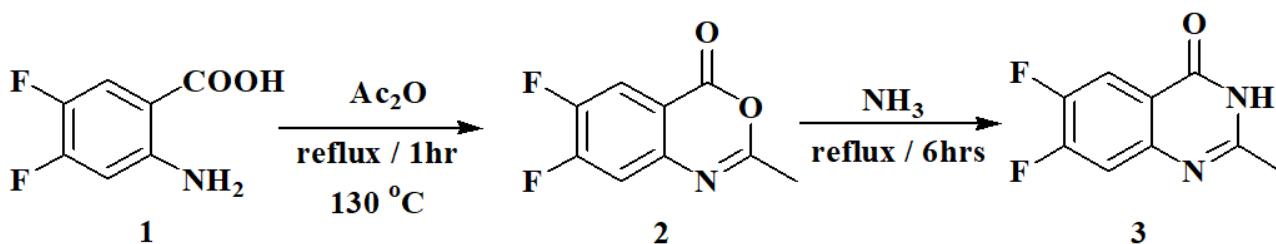
Compounds **2–7** were prepared as displayed in Schemes 1 and 3. The structures of the newly synthesized organic compounds were confirmed using ¹H, ¹³C NMR, and mass spectra.

Benzoxazinone compounds can be prepared by treatment of anthranilic acid derivatives with acid chloride [1] or acetic anhydride [2,55]. 5-dimethyl-2-thiazolyl. The 6,7-difluoro-4-benzoxazinone **2** was prepared from the reaction of 2-amino-4,5-difluorobenzoic acid **1** with acetic anhydride for 1 h. Treatment of compound **2** with ammonia solution for 6 h afforded the (3*H*)-6,7-difluoro-2-methyl-4-quinazolinone **3**, Scheme 1.

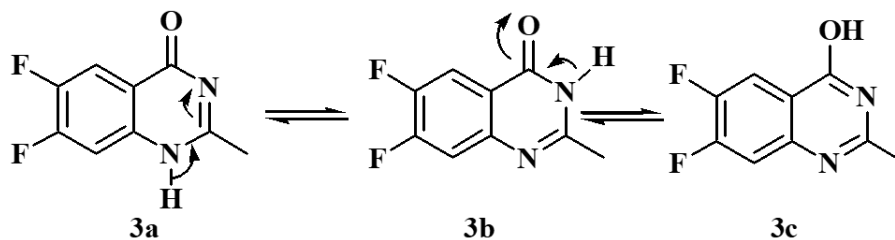
Weddige identified the tautomeric characteristics of (3*H*) 4-quinazolinones, which could exist in three tautomeric forms. The existence of 4-hydroxy quinazolinone was displayed by its stability in aqueous alkali at pH 12 to give the anion form. The 4-quinazolinones usually do not dissolve in alkali, mainly when a substitute is present on N1 or N3 [15]. The compound, 6,7-difluoro-2-methyl-4-quinazolinone is expected to have three tautomeric forms of (1*H*) 6,7-difluoro-2-methyl-4-quinazolinone **3a**, **3b**, and **3c**, Scheme 2.

Table 1. Dipole moment and chemical reactivity descriptors (Debye, μ) of the prepared compounds **3** and **7**.

Parameter	3a	3b	7
LUMO	-2.17	-1.97	-2.23
HOMO	-6.96	-6.96	-6.96
$\Delta E_{LUMO-HOMO}$	4.80	5.00	4.74
$\chi = -\frac{1}{2}(E_{HOMO} + E_{LUMO})$	4.57	4.47	4.60
$\eta = -\frac{1}{2}(E_{HOMO} - E_{LUMO})$	2.40	2.50	2.37
$\delta = \frac{1}{\eta}$	0.42	0.40	0.42
$\omega = \frac{\chi^2}{2\eta}$	4.34	3.99	4.46
$I = -E_{HOMO}$	6.96	6.96	6.96
$A = -E_{LUMO}$	2.17	1.97	2.23
μ	4.87	5.87	6.87



Scheme 1. Synthesis of nucleoside (3H)-6,7-difluoro-2-methyl-4-quinazolinone



Scheme 2. Tautomeric properties of (1H)-6,7-difluoro-2-methyl-4-quinazolinone **3a**, **3b**, and **3c**.

A mixture of **3a**, dry HMDS, and a catalytic quantity of $(\text{NH}_4)_2\text{SO}_4$ was heated under reflux for 24 h (TLC). The product was evaporated to dryness in anhydrous media to afford the silylated derivative **4** as an intermediate compound. Compound **5** was treated with trimethylsilyl triflate; (TMSOTf as a catalyst), an aqueous NaHCO_3 , and silica gel column chromatography with ethyl acetate and chloroform (2:98) to obtain **6** as a sticky yellow material. The ^1H NMR of the protected nucleoside **6** shows a doublet signal at $\delta = 6.1$ ppm allocated to the anomeric protons of the ribose moiety with a J coupling constant equal to 4.25 Hz matches the $1'$ -proton. The spectra appeared as multiple signals of the configuration at $\delta = 8.06$ – 7.13 ppm due to benzoyl groups and quinazolinone protons in an aromatic region, see Scheme 3 and Figure 1.

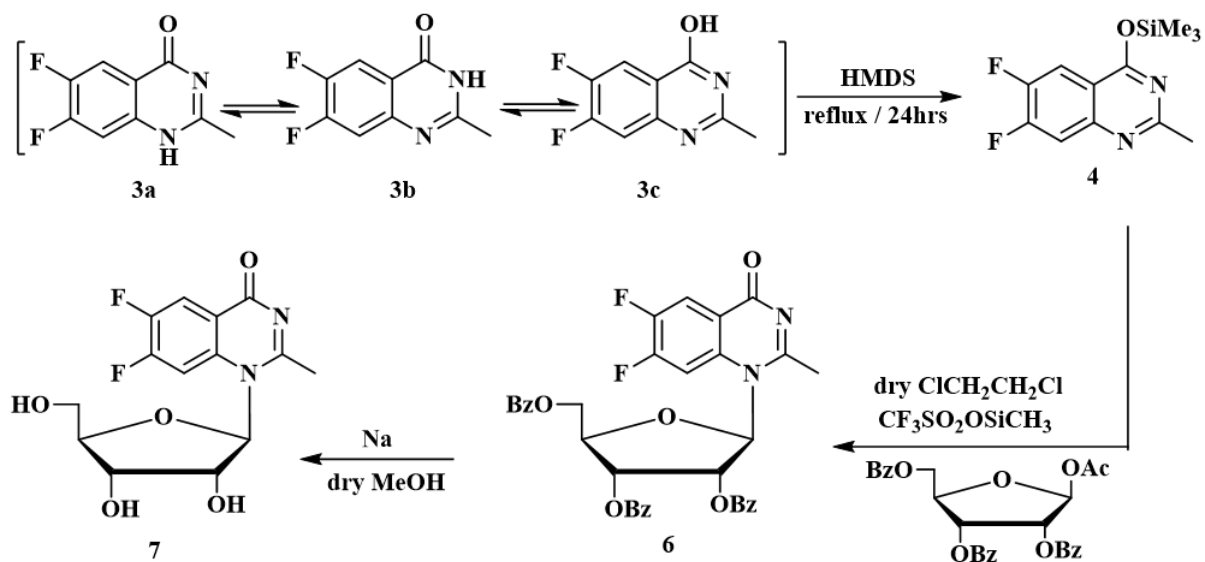
Deprotection of the benzoyl group of protected nucleoside **6** was achieved in sodium metal in dry methanol at room temperature for 24 h to give the corresponding free nucleoside **7**. The ^1H NMR of **7** showed the prospective base moiety protons and the sugar moiety protons, though no signal for benzoyl protons appeared. Also, the ^1H NMR spectrum of **7** shows a doublet at $\delta = 6.9$ ppm allocated to the anomeric proton of the ribose moiety with J coupling constant equal to 4.25 Hz that matches the $1'$ -proton the β -configuration. With the appearance of aromatic group complex signals, a singlet peak appeared at $\delta = 7.88$ ppm allocated to the H-5, and another singlet signal at $\delta = 6.94$ ppm assigned to the H-8. The ^1H NMR of **7** showed the predicted base moiety protons in addition to the sugar moiety protons. Calculated ^1H , and ^{13}C NMR of an optimized molecular geometry of compound **7** in deuterated methanol solvent are provided for comparison (Figure 1; experimental section). Compound **7** was confirmed using mass spectra which showed a molecular ion peak ion (M^+) at $m/z = 327.21$ (2.77%), (calc. 328.27) for molecular formula $\text{C}_{14}\text{H}_{14}\text{F}_2\text{N}_2\text{O}_3$, the base peak = 319.18 (100).

3.1. DFT theoretical calculations

3.1.1. Molecular geometry

The optimal molecular structures were predicted using DFT calculations at the B3LYP 6311G (d, p) basis set to assess the stability of the expected positional isomers. To estimate the most stable positional isomer of the produced compound **3**, calculations were performed for the proposed two isomers, **3a** and **3b**. These computations entailed doing a geometry structure optimization on each isomer to obtain the least energy structure, then calculating the frequency at the optimized geometry. In addition, several thermochemical parameters were calculated (Figure 2; Table 2). Free energy (G) and enthalpy (H) were calculated to determine the relative stabilities, corrected energy, and thermodynamic parameters of both positional isomers of compound **3**.

The DFT calculations revealed that the **3b** isomer had the lowest energy structure and the most stability in comparing both geometrical isomers. The **3b** isomer, on the other hand, is the least stable. The energy difference between both isomers is 11.2 kcal/mol. However, the amid derivative **3b** higher stability could be illustrated in its tautomeric ability with the conjugated $\text{C}=\text{O}$ group (Figure 3).



Scheme 3. Synthesis of nucleoside 6,7-difluoro-2-methyl-4-quinazolinone.

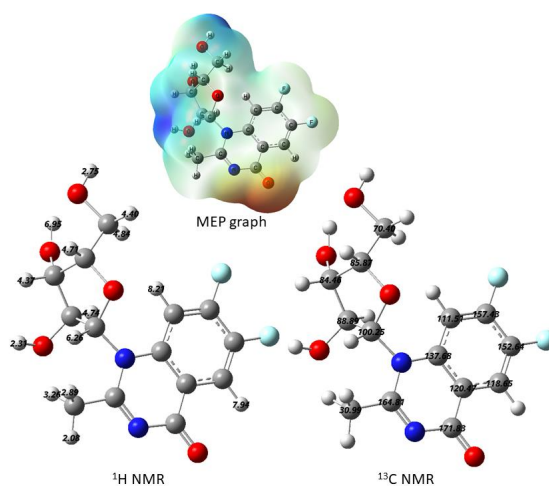


Figure 1. Calculated ^1H and ^{13}C NMR of an optimized molecular geometry of compound 7 in deuterated methanol solvent. MEP graph is also presented.

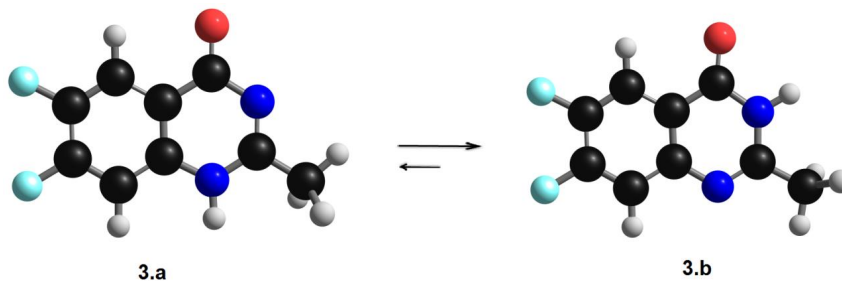
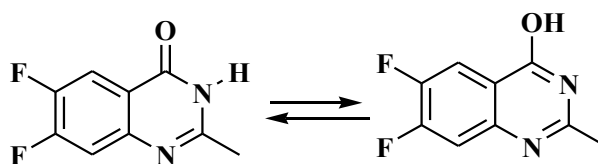


Figure 2. Calculated optimized molecular geometry of both isomers of compound 3.

Table 2. Thermal parameters (hartree/particle) of both positional isomers of compound **3**.

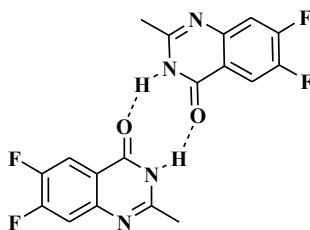
Parameter	3a	3b
E_{corr}	0.139237	0.139796
ZPVE	-730.840481	-730.858147
E_{tot}	-730.829206	-730.847069
H	-730.828262	-730.846124
G	-730.878053	-730.895234
ΔE in kcal/mol	11.209	0.00

**Figure 3.** Tautomeric isomerism of compound **3**.

On the other hand, the intermolecular H-bonding could affect the stability of the predicted stable isomer **3b**. Isomer **3b** can form intermolecular H-bonding with two strong H-bonds than the other isomer **3a**. The formation of two H-bonds will enhance the stability of the amid isomer **3b** more than the other isomer (Figure 4).

3.2. Docking analysis

This docking study investigates how a nucleoside ligand might interact in the active site of the main protease (M^{pro} ; PDB code 7BQY, 1EVE) for Alzheimer's disease and COVID-19 [15]. Hydrogen bonding, hydrophobic interactions, and other factors, e.g., entropy and solvation, can control the structural reorganization of both the ligand and the receptor upon binding. It remains challenging to predict the conformational changes of 7BQY, 1EVE, and the ligand, as both are expected to display different degrees of adjustment after binding [33]. The docked molecule in 7BQY is shown in Figure 5. The confirmation of all molecules has been demonstrated with respect to the known medicine Remdesivir Figure 5. It has been noticed that the Met165(A), Arg188(A), Gln189(A), and Gly143(A) amino acids are the common residues, forming hydrophobic interactions among all the compounds used in this study. At the same time, Remdesivir forms four hydrogen bonds (Leu141(A), Asn143(A), Ser144(A) and Glu166(A)). Similarly, compound **7** also forms 4 hydrogen bonds ((Leu141(A), Ser144(A), His163(A) and Glu166(A)). **N3** displays three hydrogen bonds (Leu41(A), Asn142(A) and His163(A)). Compounds **3a** and **3b** show one and two hydrogen bonds, respectively, Figures 6 and 7. A superposition of compounds **3a**, **3b**, **7**, remdesivir drug, and **N3** inhibitor docked into the binding pocket of 7BQY using the identical parameters for a fair comparison. The outcomes are presented in Figure 5. The number and type of interactions between the remdesivir, **N3**, **7**, **3a**, **3b** and the main protease (7BQY) are summarized in Figure 6 and partly in Figure 7. The laydown of all docked ligands is presented together (with and without 7BQY), showing their fitting in the same active site but different positioning (Figure 5). Also, the display of the superposition of each ligand compared to remdesivir is displayed for easy comparison. This is represented by PyMOL by Schrödinger [56].

**Figure 4.** Intermolecular H-bonding of amid isomer **3b**.

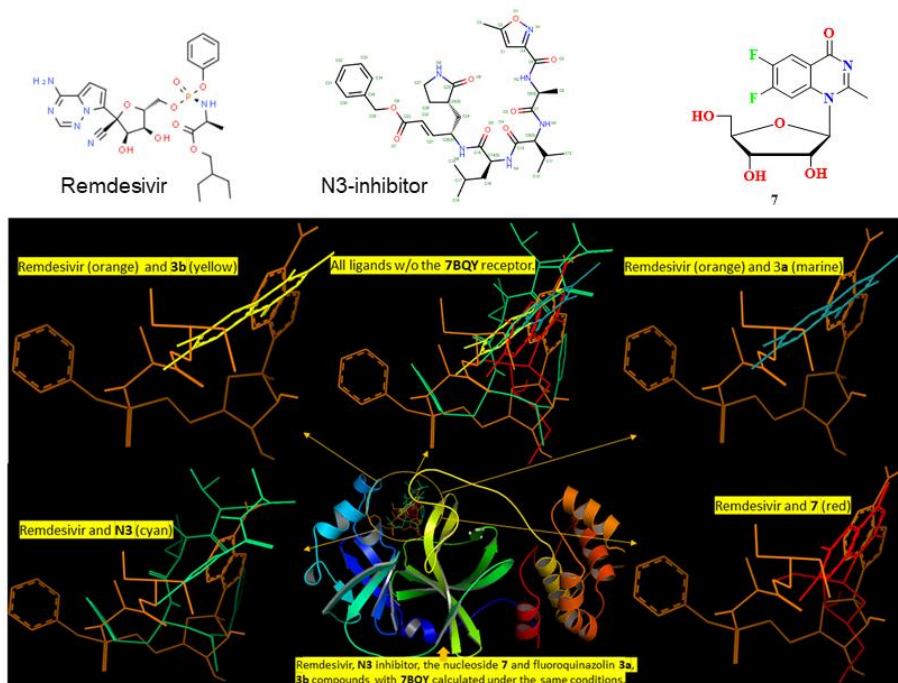


Figure 5. The superposition of compounds 3a, 3b, 7, remdesivir drug, and N3 inhibitor docked into the binding pocket of 7BQY using the identical parameters for a fair comparison (circled, middle bottom window). For clarity, all docked ligands are shown in the top central window without the 7BQY, M^{Pro}. Finally, the display of each ligand after docking is compared to remdesivir (orange in color). This is represented by PyMOL by Schrödinger (downloaded from <https://pymol.org/2/>) [56].

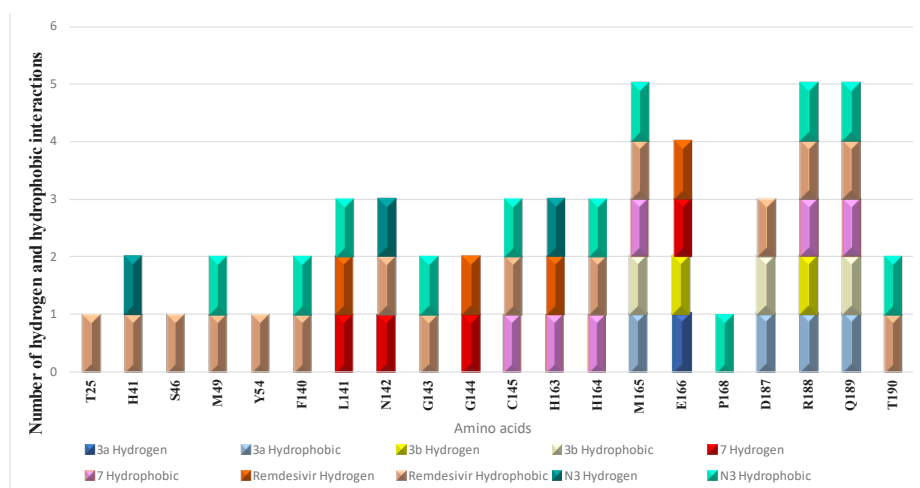


Figure 6. Number and type of interactions between the remdesivir, N3, 7, 3a, 3b, and the main protease (7BQY).

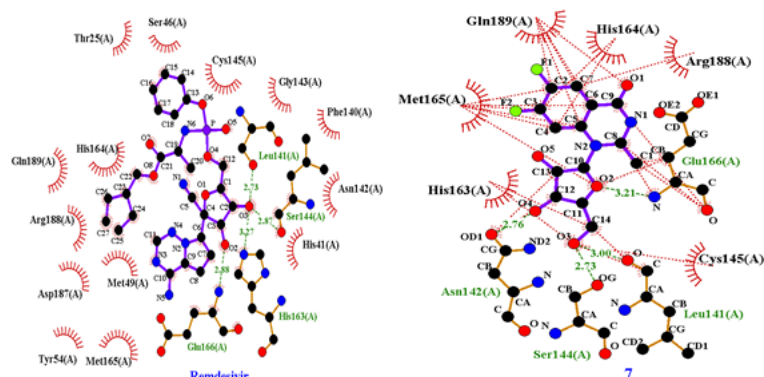


Figure 7. (a) A schematic 2D LIGPLOT illustration of remdesivir and the main protease 7BQY. The purple stick at the center represents remdesivir, whereas the remaining are the amino acids residues. The green dashes are the hydrogen bond, and the thin red dashes and the spoked arcs pointing towards the ligand represent the hydrophobic residue bonds with remdesivir. The active site residues: Leu141(A), Asn143(A), Ser144(A), and Glu166(A) are involved in making a hydrogen bond with the ligand. Atoms marked by spokes in the ligand or protein are involved in the interactions without the red lines. (b) A schematic 2D LIGPLOT illustration of compounds 7 and 7BQY represented by PyMOL [56].

3.3. Binding prediction of compound 7 compared to donepezil using molecular docking

Docking analysis of compound 7 and donepezil was carried out on the Torpedo California acetylcholinesterase to study their binding affinity (TcAChE) (PDB, 1EVE), [57–62]. Compound 7 demonstrated a close-fitting binding against the TcAChE enzyme with close binding energy of -9.7 kcal/mol compared to donepezil (-10.9 kcal/mol) (Figures 8 and 9). The molecular structure of 7 and donepezil after binding with the protein are shown in Figures 8 and 9. Compound 7 shows conventional hydrogen bonds, fluorine-hydrogen bonds, carbon-hydrogen bonds, and van der Waals interaction. In contrast, the donepezil drug does not exhibit any of these interactions, indicating probably considerable flexibility of compound 7 that facilitates the tight interaction with the binding site for the quaternary nitrogen of AChE enzyme [33]. Donepezil drug demonstrates mainly π - σ and π - π stacked interactions (Figure 9). Superimposition of 7 (blue line) and donepezil (orange line) is shown in Figure 8, which demonstrates the benzylpiperidine group oriented towards PHE, TYR, and TRP residues. Similarly, the quinazoline moiety in compound 7 is directed towards PHE, TYR, and TRP residues. The inden-1-one group of donepezil oriented towards TRP, ARG, and LEU residues (Figure 9), whereas the hydrofuran moiety in 7 is directed towards SER, TYR, and Val residues. TRP84 interacts via π -sigma interaction with a distance of 3.37 Å. In contrast, in the case of donepezil, it exhibits a π - π stacking with a distance of 4 Å (Figure 9). Three conventional hydrogen bonds were found between the hydroxyl groups and SER81, TYR70, and TYR121 residues with distances of 3.3 , 3.72 , and 5.95 Å, respectively (Figure 9). Interestingly, as can be seen, at the bottom of the gorge, a $C=O \cdots HIS440$ hydrophobic interaction was formed in the active site of AChE [63]. This interaction was not detected in the donepezil drug case. This might enhance the affinity to the enzyme and therefore improve the inhibition effect of compound 7.

3.4. Toxicity prediction (in silico) for our ligands in comparison to remdesivir and N3

ProTox-II virtual lab was used to predict the toxicity of our small molecules in comparison to the authorized drug remdesivir [64-70] and N3 inhibitor [31]. The oral toxicity presented as lethal dose (LD) at 50% (LD50) milligrams per kilograms weight of the test population. ProTox-II predicted the toxicity classes as class 3 for 3a and 3b and LD50 of 200 mg/kg with the same average similarity and prediction accuracy of 60.65% and 68.07%, respectively (Table 3). Interestingly, the toxic activity of 7 is predicted as class 4, which is similar to the approved drug, remdesivir, with LD50 of 1000 mg/kg. The average similarity and prediction accuracy of 7 and remdesivir were 66.03%, 68.07%, and 40.93%, 54.26%, respectively (Table 3). Compound N3 was predicted as the lowest toxic compound in this study as class 5 with LD50 of 4000 mg/kg and average similarity and prediction accuracy of 45.06% and 54.26, respectively (Table 3).

The ProTox-II web server can also predict organ toxicity. For example, the hepatotoxicity estimation of the three ligands 3a, 3b, the approved medicine for COVID-19 remdesivir and N3 inhibitor were all not active. In contrast, 7 was predicted as a functional ligand on organ toxicity (Lever) with a probability of 0.52. Predicted activities for all studied ligands and the controls (remdesivir and N3) were inactive (noncarcinogenic, non immunotoxin, nonmutagenic, noncytotoxic) (Table 4).

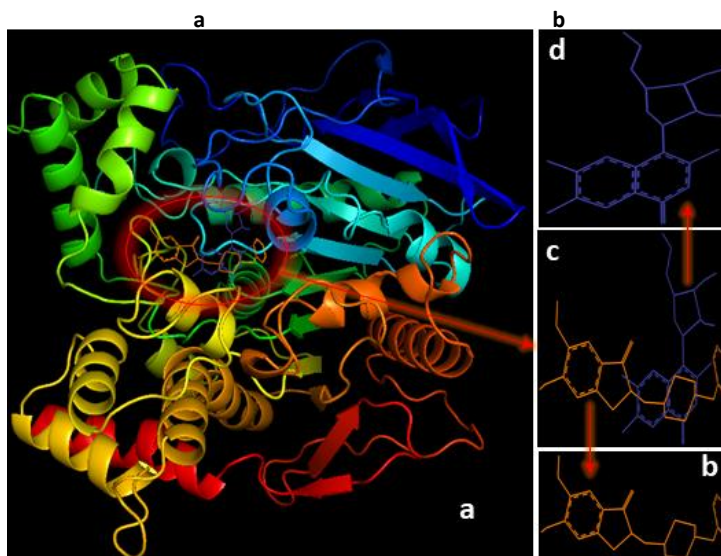


Figure 8. (a) The superposition of compound 7 and donepezil docked to 1EVE using the identical parameter for a reasonable comparison; (b) the display of donepezil drug after docking; (c) the display of both donepezil drug and compound 7; (d) the display of compound 7. Results are presented using PyMOL [56].

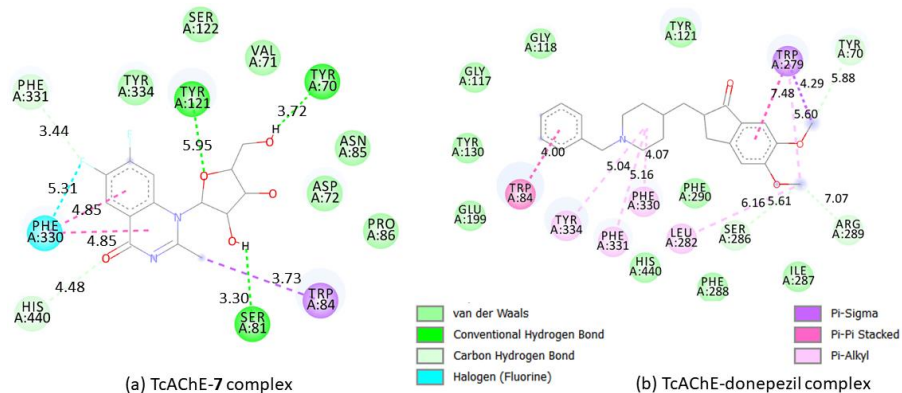


Figure 9. 2D representations of interactions in (a) TcAChE- 7 complex; (b) in TcAChE-donepezil complex. Distances are in Å°.

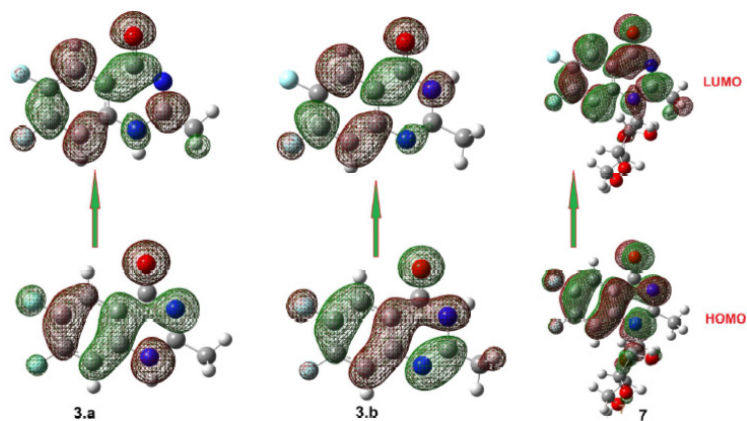
Figure 10 depicts the prediction of the FMOs energy levels and their energy gap of **3a** and **3b** and its nucleoside **7**. The energy levels of the FMOs in compound **3a** are lower than those in compound **3b**, which could be explained in terms of conjugation. The presence of an H-atom adjacent to the C=O group enhances the tautomerism with the OH. It may decrease the conjugation of the C=O group with the ring, inhibiting the conjugation with the benzene ring. This effect on MO levels has an impact on the chemical descriptors that are used to illustrate the biological activity of these compounds. However, the attachment of the hydrophilic carbohydrate moiety of the isomer **3a** affects the energy difference between the orbitals with a small value $\Delta E = 4.74$ e.V. Also, it is evident that the isomerism highly affects the level of the LUMO than the HOMO. Isomer **3b** shows the lowest-lying LUMO. The low-lying LUMO orbital of **3b** could predict its ability to accept the electron than its tautomer and its nucleoside derivative **7**. However, the higher topological, polar surface area, lower hydrophobicity, in silico absorption and high H-bonding acceptor percent of compound **7** could illustrate its high predicted biological activity against the inhibition of COVID 19 and Alzheimer infections.

Table 3. Acute oral toxicity predicted by ProTox-II web server for ligands **3a**, **3b**, **7**, remdesivir, and **N3**.

Ligands drug and N3	Oral toxicity prediction results			
	Predicted LD50 (mg/kg)	Predicted toxicity class	Average similarity (%)	Prediction accuracy (%)
3a	200	3	60.65	68.07
3b	200	3	60.65	68.07
7	1000	4	66.03	68.07
Remdesivir	1000	4	40.93	54.26
N3	4000	5	45.06	54.26

Table 4. Organ toxicity and toxicological endpoints predicted activity calculated using the ProTox-II web server for ligands **3a**, **3b**, **7**, remdesivir, and **N3**.

Ligands drug and N3	Hepatotoxicity		Carcinogenicity		Immunotoxicity		Mutagenicity		Cytotoxicity	
	Activity	Probability	Activity	Probability	Activity	Probability	Activity	Probability	Activity	Probability
3a	x	0.54	x	0.51	x	0.99	x	0.64	x	0.90
3b	x	0.54	x	0.51	x	0.97	x	0.64	x	0.90
7	√	0.52	x	0.66	x	0.96	x	0.77	x	0.77
Remdesivir	x	0.56	x	0.55	x	0.90	x	0.62	x	0.55
N3	x	0.58	x	0.52	x	0.96	x	0.61	x	0.67

**Figure 10.** Molecular orbital distribution and localization for FMOs of **3a**, **3b**, and **7**.

4. Conclusions

Synthesis of some of the ribosylation of silylated compound **4** with 1-*O*-acetyl-2,3,5-tri-*O*-benzoyl- β -D-ribofuranose **5** gave β -anomeric of the benzoylated nucleoside derivatives **6**. Deprotection of the latter using dry absolute methanol and sodium metal gave the new free N-nucleosides **7**, in moderate yields. The new compounds obtained have been characterized by their spectral analysis. The prediction analysis using the Pro Tox -II server showed that compound **7** has a similar feature to the approved antiviral drug remdesivir for COVID-19. Compound **7** behaved similarly in all tests except on hepatotoxicity. This suggests that compound **7** may be worth additional study in the context of a possible drug for COVID-19. A molecular modeling investigation confirmed, in silico, that our nucleosides **7** is an excellent binding

inhibition of AChE enzyme. Compound 7 could be a possible effective drug against Alzheimer's disease. Finally, DFT was used to demonstrate molecular geometry and the thermodynamic parameters that could be used to illustrate the MD results in terms of the structural activity correlation computed from FMOs using molecular descriptors. Compound 7 demonstrated its predicted activity towards binding inhibition of AChE enzyme and Alzheimer's disease due to higher hydrophilicity, a larger topological polar surface area, and a strong H-bonding acceptor.

Funding

This research was funded by Researchers Supporting project Taif, Kingdom of Saudi Arabia (KSA, grant number TURSP-2020/137).

Acknowledgments

The authors thank Taif University, Taif University Researchers Supporting project number (TURSP-2020/137), Taif University, Taif, Kingdom of Saudi Arabia (KSA). MAS is thankful to the Alexander von Humboldt Foundation for its continuous support.

Conflict of interest

The authors declare no conflicts of interest. The funders had no role in the design of the study, in the collection, analyses, or interpretation of data, in the writing of the manuscript, or in the decision to publish the results.

References

1. Santagati NA, Bousquet E, Spadaro A, Ronsisvalle G. 4-Quinazolinones: Synthesis and reduction of prostaglandin E2 production. *Farmaco* 1999; 54: 780–784. doi: 10.1016/S0014-827X(99)00102-0
2. Zayed MF, Ahmed HEA, Ihmaid S, Omar ASM, Abdelrahim AS. Synthesis and screening of somenew fluorinated quinazolinone-sulphonamide hybrids as anticancer agents. *Journal of Taibah University Medical Sciences* 2015; 10: 333–339. doi: 10.1016/j.jtumed.2015.02.007
3. Singhal TA Review of Coronavirus Disease-2019 (COVID-19). *Indian Journal of Pediatrics* 2020; 87: 281–286. doi: 10.1007/S12098-020-03263-6
4. Radwan AA, Alanazi FK. Biological Activity of Quinazolinones, IntechOpen 2020. DOI: 10.5772/intechopen.90621
5. Poorirani S, Sadeghian-Rizi S, Khodarahmi G, Khajouei M, Hassanzadeh F. Synthesis and cytotoxic evaluation of novel quinazolinone derivatives as potential anticancer agents. *Research in Pharmaceutical Sciences* 2018; 13: 450. doi:10.4103/1735-5362.236838
6. Gawad N, Georgey H, Youssef R, El-Sayed N. Synthesis and antitumor activity of some 2, 3-disubstituted quinazolin-4 (3H)-ones and 4,6-disubstituted-1, 2,3,4-tetrahydroquinazolin-2H-ones. *European Journal of Medicinal Chemistry* 2010; 45: 6058–6067.
7. Andreeva OV, Belenok MG, Saifina LF, Shulaeva MM, Dobrynin AB et al. Synthesis of novel 1,2,3-triazolyl nucleoside analogues bearing uracil, 6-methyluracil, 3,6-dimethyluracil, thymine, and quinazoline-2,4-dione moieties. *Tetrahedron Letters* 2019; 60.
8. Abdel Gawad NM, Georgey HH, Youssef RM, El-Sayed NA. Synthesis and antitumor activity of some 2, 3-disubstituted quinazolin-4(3H)-ones and 4,6-disubstituted- 1,2,3,4-tetrahydroquinazolin- 2H-ones. *European Journal of Medicinal Chemistry* 2010; 45: 6058–6067. doi:10.1016/j.ejmech.2010.10.008
9. Rajput C, Singhal S. Synthesis, characterization, and antiinflammatory activity of newer quinazolinone analogs, Downloads.Hindawi. Com 2013. *Journal of pharmaceutics* 2013; 2013: 1–7. doi:10.1155/2013/907525
10. Gatadi S, Lakshmi TV, Nanduri S. 4(3H)-Quinazolinone derivatives: Promising antibacterial drug leads. *European Journal of Medicinal Chemistry* 2019; 170: 157–172. doi:10.1016/J.EJMECH.2019.03.018
11. Sharaf A, Ragab S, Elbarbary A, Elkhabyry S. Synthesis and biological evaluation of some 3H-quinazolin-4-one derivatives. Springer 2021; doi:10.1007/s13738-021-02315-8
12. Zhang J, Liu J, Ma Y, Ren D, Cheng P et al. One-pot synthesis and antifungal activity against plant pathogens of quinazolinone derivatives containing an amide moiety. *Bioorganic Medicinal Chemistry Letters* 2016; 26: 2273–2277. doi:10.1016/J.BMCL.2016.03.052
13. Asif M. Chemical Characteristics, Synthetic Methods, and Biological Potential of Quinazoline and Quinazolinone Derivatives. *International Journal of Medicinal Chemistry* 2014; 2014: 1–27. doi:10.1155/2014/395637
14. Demeunynck M, Baussanne I. Survey of Recent Literature Related to the Biologically Active 4(3H)-Quinazolinones Containing Fused Heterocycles. *Current Medicinal Chemistry* 2013; 20: 794–814. doi:10.2174/0929867311320060006

15. Zahlenreilien L, Lage D, I. Ueber. Beitrage zur Kenntniss. Journal Für Praktische. Chemie 1887; 141–154 (in German).
16. Foucourt A, Hédou D, Dubouilh-Benard C, Girard A, Taverne T et al. Design and Synthesis of Thiazolo[5,4-f]quinazolines as DYRK1A Inhibitors, Part I. *Molecules* 2014;19: 15546–15571.
17. Foucourt A, Hédou D, Dubouilh-Benard C, Girard A, Taverne T et al. Design and synthesis of thiazolo[5,4-f]quinazolines as DYRK1A inhibitors, Part II, *Molecules* 2014; 19: 15411–15439. doi:10.3390/molecules191015411
18. Couly F, Diharce J, Bonnet P, Meijer L, Fruit C, Besson T. Conception of DYRK1A kinase inhibitors via metal-catalyzed C–H arylation, inspired by fragment-growing studies, in 4th International Electronic Conference on Medicinal Chemistry 2018; p. 5580. doi:10.3390/ecmc-4-05580
19. Shah P, Westwell AD. The role of fluorine in medicinal chemistry. *Journal of Enzyme Inhibition and Medicinal Chemistry* 2007; 22: 527–540. doi:10.1080/14756360701425014
20. Ghorab MM, Abdel-Gawad SM, El-Gaby MSA. Synthesis and evaluation of some new fluorinated hydroquinazoline derivatives as antifungal agents. *Farmaco* 2000; 55: 249–255. doi:10.1016/S0014-827X(00)00029-X
21. Layeva AA, Nosova EV, Lipunova GN, Trashakhova TV, CharushinVN. A new approach to fluorinated 4(3H)-quinazolinones. *Journal of Fluorine Chemistry* 2007; 128: 748–754. doi:10.1016/j.jfluchem.2007.03.005
22. Akher FB, Farrokhzadeh A, Ravenscroft N, Kuttel MM. Mechanistic Study of Potent Fluorinated EGFR Kinase Inhibitors with a Quinazoline Scaffold against L858R/T790M/C797S Resistance Mutation: Unveiling the Fluorine Substituent Cooperativity Effect on the Inhibitory Activity. *Journal of Physical Chemistry B* 2020; 124: 5813–5824. doi:10.1021/ACS.JPCB.0C03440
23. Break LM, Alharthi W. Synthesis new of nucleoside of 1, 3-bis-(2,3,5-tri-O-benzoyl-β-D-ribofuranosyl)-8-(trifluoromethyl)-2-methyl-4-quinazolinone. *Proceedings* 2018; 9: 57. doi:10.3390/ecsoc-22-05694
24. Break LM. Synthesis of 8-Trifluoromethyl-2-Thioquinazolin-(3H)-4-One Nucleosides, *International Journal Chemistry* 2017; 9: 82. doi:10.5539/ijc.v9n4p82
25. Break LM. Synthesis and Characterization of New 8-trifluoromethyl Quinazolin-2,4-(3H)-Dione Nucleosides *International Journal Chemistry* 2017; 9: 73. doi:10.5539/ijc.v9n1p73
26. Break LM. Synthesis of Some of Fluorinated Benzimidazole Nucleosides. *International Journal Chemistry* 2016; 8: 188. doi:10.5539/ijc.v8n1p188
27. Ouahrouch A, Taourirte M, Engels JW, Benjelloun S, Lazrek HB. Synthesis of new 1,2,3-triazol-4-yl-quinazoline nucleoside and acyclonucleoside analogues. *Molecules* 2014; 19: 3638–3653. doi:10.3390/molecules19033638
28. Qiu J, Chen W, Zhang Y, Zhou Q, Chen J et al. Assessment of quinazolinone derivatives as novel non-nucleoside hepatitis B virus inhibitors. *European Journal of Medicinal Chemistry* 2019; 176: 41–49. doi:10.1016/J.EJMECH.2019.05.014
29. Laeva AA, Nosova EV, Lipunova GN, Golovchenko AV, Adonin NY et al. Fluorine-containing heterocycles: XIX. synthesis of fluorine-containing quinazolin-4-ones from 3,1-benzoxazin-4-ones. *Russian Journal of Organic Chemistry* 2009; 45: 913–920. doi:10.1134/S1070428009060190
30. Vorbrüggen H, Krolkiewicz K, Benna B. Nucleoside syntheses, XXII Nucleoside synthesis with trimethylsilyl triflate and perchlorate as catalysts. *Chemische Berichte* 1981; 114: 1234–1255. doi:10.1002/cber.19811140404
31. Jin Z, Du X, Xu Y, Deng Y, Liu M et al. Structure of Mpro from SARS-CoV-2 and discovery of its inhibitors. *Nature* 2020; 582: 289–293. doi:10.1038/s41586-020-2223-y
32. Dhama K, Sharun K, Tiwari R, Dadar M, Singh Malik Y et al. COVID-19, an emerging coronavirus infection: advances and prospects in designing and developing vaccines, immunotherapeutics, and therapeutics. *Human Vaccines & Immunotherapeutics* 2020; 16: 1232–1238. doi:10.1080/21645515.2020.1735227
33. Alsafi MA, Hughes DL, Said MA. First COVID-19 molecular docking with a chalcone-based compound: Synthesis, single-crystal structure and Hirshfeld surface analysis study. *Acta Crystallographica Section: C Structural Chemistry* 2020; 76: 1043–1050. doi:10.1107/S2053229620014217
34. Fan X, Zhang X, Zhou L, Keith KA, Kern ER et al. A pyrimidine-pyrazolone nucleoside chimera with potent in vitro anti-orthopoxvirus activity. *Bioorganic & Medicinal Chemistry Letters* 2006; 16: 3224–3228. doi:10.1016/j.bmcl.2006.03.043
35. Wang CX, Zhang ZL, Yin QK, Tu JL, Wang JE et al. Design, Synthesis, and Evaluation of New Quinazolinone Derivatives that Inhibit Bloom Syndrome Protein (BLM) Helicase, Trigger DNA Damage at the Telomere Region, and Synergize with PARP Inhibitors. *Journal Medicinal Chemistry* 2020; 63: 9752–9772. doi:10.1021/ACS.JMEDCHEM.0C00917/SUPPL_FILE/JM0C00917_SI_002.CSV
36. Allouche A, Khodair AI, El-Barbary AA, Imam DR, Kheder NA et al. Software News and Updates Gabedit — A Graphical user interface for computational Chemistry softwares. *Journal of Computational Chemistry* 2012; 32: 174–182. doi:10.1002/jcc

37. Wallace AC, Laskowski RA, Thornton JM. Ligplot: A program to generate schematic diagrams of protein-ligand interactions. *Protein Engineering Design and Selection* 1995; 8: 127–134. doi:10.1093/protein/8.2.127
38. Al-Otaibi JS, Sheena Mary Y, Shyma Mary Y, Panicker CY, Thomas R. Cocrystals of pyrazinamide with p-toluenesulfonic and ferulic acids: DFT investigations and molecular docking studies. *Journal Molecular Structure* 2019; 1175: 916–926. doi:10.1016/J.MOLSTRUC.2018.08.055
39. Hagar M, Ahmed HA, Aljohani G, Alhaddad OA. Investigation of some antiviral N-heterocycles as COVID 19 drug: Molecular docking and DFT calculations. *International Journal of Molecular Sciences* 2020; 21: 3922. doi:10.3390/ijms21113922
40. Pap C, Mohapatra RK, El-ajaily MM, Alassbaly FS, Sarangi AK et al. DFT, anticancer, antioxidant and molecular docking investigations of some ternary Ni (II) complexes with 2- phenol. *Springer* 2021; 75: 1005–1019. doi:10.1007/s11696-020-01342-8
41. Bouachrine M, Hamidi M, Bouzzine SM, Taoufik H. Theoretical study on the structure and electronic properties of new materials based on thiophene and oxadiazole. *Journal of Applied Chemical Research* 2009; 10: 29–37. <https://www.sid.ir/en/Journal/ViewPaper.aspx?ID=195555>
42. Yang L, Feng JK, Liao Y, A.M. Ren QM. Theoretical studies on the electronic and optical properties of two blue-emitting fluorene-pyridine-based copolymers. *Optical Materials* 2007; 29: 642–650. doi:10.1016/j.optmat.2005.11.024
43. Alnoman RB, Parveen S, Hagar M, Ahmed HA, Knight JG. A new chiral boron-dipyrromethene (BODIPY)-based fluorescent probe: molecular docking, DFT, antibacterial and antioxidant approaches. *Journal. Biomolecular Structure and Dynamis* 2020; 38: 5429–5442. doi:10.1080/07391102.2019.1701555.
44. Alnoman RB, Hagar M, Parveen S, Ahmed HA, Knight JG. Computational and molecular docking approaches of a New axially chiral BODIPY fluorescent dye. *Journal of Photochemistry and Photobiology A: Chemistry* 2020; 395: 112508. doi:10.1016/j.jphotochem.2020.112508
45. Joshi R, Pandey N, Yadav SK, Tilak R, Mishra H et al. Synthesis, spectroscopic characterization, DFT studies and antifungal activity of (E)-4-amino-5-[N²-(2-nitro-benzylidene)-hydrazino]-2,4-dihydro-[1,2,4]triazole-3-thione. *Journal Molecular Structure* 2018; 1164: 386–403. doi:10.1016/j.molstruc.2018.03.081
46. Joshi R, Kumari A, Singh K, Mishra H, Pokharia S. Triorganotin(IV) complexes of Schiff base derived from 1,2,4-triazole moiety: Synthesis, spectroscopic investigation, DFT studies, antifungal activity and molecular docking studies. *Journal Molecular Structure* 2020; 1206: 127639. doi:10.1016/j.molstruc.2019.127639
47. Khodair AI, Awad MK, Gesson JP, Elshaier YAM. New N-ribosides and N-mannosides of Rhodamine Derivatives for Suppressing Leukemia Cell Line Growth. *Journal Clinical Haematology* 2020; 1: 7–9. doi:10.33696/haematology.1.002
48. Suresh Kumar S, Athimoolam S, Sridhar B. Structural, spectral, theoretical and anticancer studies on new co-crystal of the drug 5-fluorouracil. *Journal Molecular Structure* 2018; 1173: 951–958. doi:10.1016/j.molstruc.2018.07.079
49. Hagar M, Ahmed HA, El-Sayed TH, Alnoman R. Mesophase behavior and DFT conformational analysis of new symmetrical diester chalcone liquid crystals. *Journal of Molecular Liquids* 2019; 285: 96–105. doi:10.1016/j.molliq.2019.04.083
50. Grover M, Singh B, Bakshi M, Singh S. Quantitative structure-property relationships in pharmaceutical research - Part 2. *Pharmaceutical Science and Technology Today* 2000; 3: 50–57. doi:10.1016/S1461-5347(99)00215-1
51. Malhotra R, Ravesh A, Singh V. Synthesis, characterization, antimicrobial activities, and QSAR studies of organotin(IV) complexes, Phosphorus, Sulfur and Silicon Related Elements 2017; 192: 73–80. doi:10.1080/10426507.2016.1225054
52. Kumer A, Sarker Md. N, Paul S. The simulating study of HOMO, LUMO, thermophysical and quantitative structure of activity relationship (QSAR) of some anticancer active ionic liquids. *Eurasian Journal of Environmental Research* 2019; 3: 1-10. <https://dergipark.org.tr/en/pub/ejere/478362>
53. Lewis DFV. Quantitative structure-activity relationships (QSARs) within the cytochrome P450 system: QSARs describing substrate binding, inhibition and induction of P450s. *Inflammopharmacology* 2003; 11: 43–73. doi:10.1163/156856003321547112
54. Almeahmadi MA, Aljuhani A, Alraqa SY, Ali I, Rezki N, Aouad MR, Hagar M. Design, synthesis, DNA binding, modeling, anticancer studies and DFT calculations of Schiff bases tethering benzothiazole-1,2,3-triazole conjugates. *Journal Molecular Structure* 2021; 1225: 129148. doi:10.1016/j.molstruc.2020.129148
55. Jiang JB, Hesson DP, Dusak BA, Dexter DL, Kang GJ et al. Synthesis and biological evaluation of 2-styrylquinazolin-4(3H)-ones, a new class of antimetabolic anticancer agents which inhibit tubulin polymerization. *Journal Medicinal Chemistry* 1990; 33: 1721–1728. <https://pubs.acs.org/doi/pdf/10.1021/jm00168a029>
56. DeLano WL. *PyMOL Reference Guide*, Delano Sci. San Carlos, CA, US. 2004; 1–68.
57. Sulimov VB, Kutov DC, Taschilova AS, Ilin IS, Tyrtysnikov EE, Sulimov AV. Docking Paradigm in Drug Design. *Current Topics in Medicinal Chemistry* 2021; 21 (6): 507–546. doi: 10.2174/1568026620666201207095626

58. Pant S, Singh M, Ravichandiran V, Murty USN, Hemant Kumar Srivastava H K. Peptide-like and small-molecule inhibitors against Covid-19. *Journal of Biomolecular Structure and Dynamics* 2021; May 39 (8): 2904-2913. doi: 10.1080/07391102.2020.1757510
59. Sonmez F, Kurt BZ, Gazioglu I, Basile L, Dag A, Cappello V, Ginex T, Kucukislamoglu M, Sonmez F, Kurt BZ, Gazioglu I, Basile L, Cappello V, Ginex T, Kucukislamoglu M, Guccione S. Design , synthesis and docking study of novel coumarin ligands as potential selective acetylcholinesterase inhibitors. *Journal Enzyme Inhibition and Medicinal Chemistry* 2017; 32(1): 285-297. doi:10.1080/14756366.2016.1250753
60. Karakaya S, Koca M, Volkan Yılmaz S, Yıldırım K, Pınar NM et al. Molecular docking studies of coumarins isolated from extracts and essential oils of zosima absinthifolia link as potential inhibitors for alzheimer's disease. *Molecules* 2019; 24: 722. doi:10.3390/molecules24040722.
61. Bajda M, Więckowska A, Hebda M, Guziar N, Sotriffer CA et al. Structure-based search for new inhibitors of cholinesterases. *International Journal of Molecular Sciences* 2013; 14: 5608–5632. doi:10.3390/ijms14035608
62. Qin J, Lan W, Liu Z, Huang J, Tang H et al. Synthesis and biological evaluation of 1, 3-dihydroxyxanthone mannich base derivatives as anticholinesterase agents. *Chemistry Central Journal* 2013; 7: <https://www.sciencedirect.com/science/article/pii/S0022286020314708> (accessed November 25, 2021).
63. Brown AD, Clegg MT, Kahler AL, Weir BS, Chang TT et al. Policy Statement on Cooperative Research and Development Agreements and Intellectual Property Licensing, *Sci. Technol* 1990; 167: 2264. Peele KA, Potla Durthi C, Srihansa T, Krupanidhi S, Ayyagari VS et al. Molecular docking and dynamic simulations for antiviral compounds against SARS-CoV-2: A computational study. *Informatics in Medicine Unlocked* 2020; 19: 100345. doi:10.1016/j.imu.2020.100345
65. Gavriatopoulou M, Ntanasis-Stathopoulos I, Korompoki E, Fotiou D, Migkou M et al. Emerging treatment strategies for COVID-19 infection. *Clinical and Experimental Medicine* 2021; 21 (2): 167-179. doi: 10.1007/s10238-020-00671-y
66. Rosenberg K. Remdesivir in The Treatment of COVID-19. *American Journal of Nursing* 2021; Jan 1, 121(1): 55. doi: 10.1097/01.NAJ.0000731668.01845.8c
67. Yousefi H, Mashouri L, Okpechi SC, Alahari N, Alahari SK. Repurposing existing drugs for the treatment of COVID-19/SARS-CoV-2 infection: A review describing drug mechanisms of action. *Biochemical Pharmacology* 2021; 183: 114296. doi: 10.1016/j.bcp.2020.114296
68. Mhatre S, Naik Sh, Patravale V. A molecular docking study of EGCG and theaflavin digallate with the druggable targets of SARS-CoV-2. *Computers in Biology and Medicine* 2021; Feb129: 104137. doi: 10.1016/j.compbiomed.2020.104137.
69. Crampon K, Giorkallos A, Deldossi M. Stéphanie Baud, Luiz Angelo Steffanel, Machine-learning methods for ligand-protein molecular docking. *Drug Discovery Today* 2022; Jan 27 (1): 151-164. doi: 10.1016/j.drudis.2021.09.007
70. Talluri S. Molecular Docking and Virtual Screening Based Prediction of Drugs for COVID-19. *Combinatorial Chemistry & High Throughput Screening* 2021; 24 (5): 716-728. doi: 10.2174/1386207323666200814132149